The Astrophysical Journal, 887:16 (12pp), 2019 December 10 https://doi.org/10.3847/1538-4357/ab4d58

The Diffuse Ionized Gas Halo of the Small Magellanic Cloud

B. M. Smart[1,2], L. M. Haffner[1,3,4], K. A. Barger[5], A. Hill[4,6,7], and G. Madsen[8]
[1] Department of Astronomy, University of Wisconsin-Madison, Madison, WI 53706, USA; bsmart@astro.wisc.edu
[2] Department of Physics, Astronomy, and Mathematics, University of Hertfordshire, Hatfield, AL10 9AB, UK
[3] Department of Physics and Astronomy, Embry-Riddle Aeronautical University, Daytona Beach, FL 32114-3900, USA
[4] Space Science Institute, Boulder, CO 80301, USA
[5] Department of Physics and Astronomy, Texas Christian University, Fort Worth, TX 76129, USA
[6] Department of Physics and Astronomy, University of British Columbia, Vancouver, BC V6T 1Z1, Canada
[7] Dominion Radio Astrophysical Observatory, Herzberg Program in Astronomy and Astrophysics, National Research Council Canada, Penticton, BC, Canada
[8] Institute of Astronomy, University of Cambridge, Madingley Road, Cambridge, CB3 0HA, UK
Received 2018 November 28; revised 2019 September 18; accepted 2019 October 5; published 2019 December 5

Abstract

Observations with the Wisconsin Hα Mapper reveal a large, diffuse ionized halo that surrounds the Small Magellanic Cloud (SMC). We present the first kinematic Hα survey of an extended region around the galaxy, from $(\ell, b) = (289\overset{\circ}{.}5, -35\overset{\circ}{.}0)$ to $(315\overset{\circ}{.}1, -5\overset{\circ}{.}3)$ and covering $+90 \leqslant v_{\rm LSR} \leqslant +210$ km s^{-1}. The ionized gas emission extends far beyond the central stellar component of the galaxy, reaching similar distances to that of the diffuse neutral halo traced by 21 cm observations. Hα emission extends several degrees beyond the sensitivity of current H I surveys toward smaller galactic longitudes and more negative galactic latitudes. The velocity field of the ionized gas near the SMC appears similar to the neutral halo of the galaxy. Using the observed emission measure as a guide, we estimate the mass of this newly revealed ionized component to be roughly (0.8–1.0) $\times$ 10^9 $M_\odot$, which is comparable to the total neutral mass in the same region of (0.9–1.1) $\times$ 10^9 $M_\odot$. We find ratios of the total ionized gas mass divided by the total neutral plus ionized gas mass in three distinct subregions to be: (1) 46%–54% throughout the SMC and its extended halo, (2) 12%–32% in the SMC Tail that extends toward the Magellanic Bridge, and (3) 65%–79% in a filament that extends away from the SMC toward the Magellanic Stream. This newly discovered, coherent Hα filament does not appear to have a well-structured neutral component and is also not coincident with two previously identified filaments traced by 21 cm emission within the Stream.

Key words: galaxies: ISM – Magellanic Clouds – galaxies: structure – ISM: kinematics and dynamics – ISM: structure

1. Introduction

The Small Magellanic Cloud (SMC) is a nearby, low-mass irregular galaxy with a gas-rich interstellar medium (ISM). As a member of an interacting system that includes the Large Magellanic Cloud (LMC), Small Magellanic Cloud, and the Milky Way (MW), the SMC has undergone interactions that have created an extended envelope of gas (Gardiner et al. 1994; Gardiner & Noguchi 1996; Besla et al. 2007). The extent of the H I envelope has been thoroughly studied (Hindman et al. 1963; Stanimirovic et al. 1999; Stanimirović et al. 2004; Brüns et al. 2005; Kalberla et al. 2005; Nidever et al. 2010) with the total neutral gas mass of the galaxy measured to be 4.0 $\times$ 10^8 $M_\odot$ (Brüns et al. 2005). However, studies of the ionized portion of the gas have been primarily limited to H II regions, supernovae remnants (SNRs), large filamentary structures (Le Coarer et al. 1993), or to the SMC Tail (Barger et al. 2013, hereafter BHB13). The Magellanic Cloud Emission-line Survey (MCELS) is the most recent imaging survey of the SMC in Hα, spanning a $4\overset{\circ}{.}5 \times 3\overset{\circ}{.}5$ region (Winkler et al. 2015). Compared to the extent of the H I envelope, MCELS surveyed the ionized gas in the central region of the galaxy and does not trace the diffuse emission from the warm ionized medium (WIM; see Figure 1).

For many active star-forming galaxies, a considerable amount of total ionized gas mass is contained in the WIM (conventionally called diffuse ionized gas (DIG) in external galaxies) and gives us insight into the radiation flowing through the galaxy (Rossa & Dettmar 2000, 2003a, 2003b; Zurita et al. 2000). As is apparent from our own Milky Way's (MW) WIM, DIG is pervasive beyond H II regions and SNRs (Haffner et al. 2003, 2009; Hill et al. 2012; Krishnarao et al. 2017) and can extend far beyond the limits of the detectable neutral gas. In the MW, the WIM has a filling factor of up to ~30% (Reynolds 1977; Berkhuijsen 1998; Gaensler et al. 2008; Savage & Wakker 2009; Hill et al. 2014; Krishnarao et al. 2017) that is dependent on the scale height. Emission is visible in every direction from our location in the Galaxy (Haffner et al. 2003). Its pervasive presence lends insight into the source of ionization and the structure of the ISM. However, it is difficult to get a complete census of the WIM in the MW and identify the sources of its ionization due to our vantage point. Nearby galaxies, like the SMC, give us a chance to view the global distribution of the WIM in a galaxy and its collective sources of ionization from an outside perspective.

As few studies have explored the extended DIG of low-mass galaxies, it is uncertain how closely the physical properties and the ionization conditions of their gas resembles that of the MW. There are a limited number of studies on the DIG in dwarf irregular galaxies that used aperture photometry (Hunter & Gallagher 1990, 1992; Hunter et al. 1993) or slit spectroscopy (Domgoergen & Dettmar 1997; Martin & Kennicutt 1997) to measure Hα emission. Hunter & Gallagher (1990) found that 15%–20% of the Hα flux emitted from dwarf irregular galaxies is from the diffuse ionized medium. Using assumptions of the properties of the DIG, they suggest that diffuse material is the dominant form of ionized gas in dwarf irregulars. However, these surveys were primarily limited to bright structures within the galaxies rather than the faint portion of the DIG. This restriction to dense

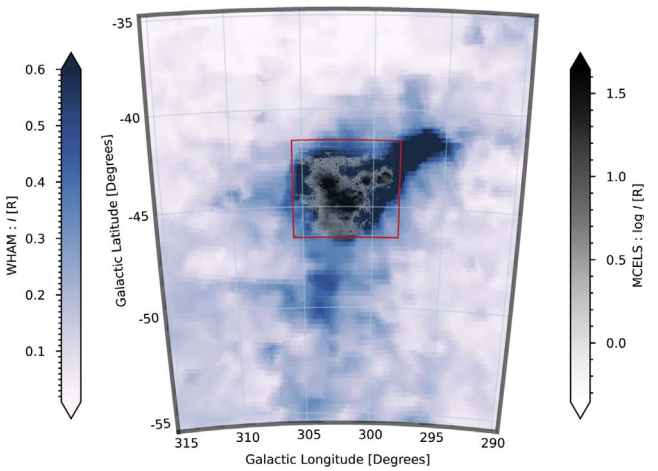

Figure 1. WHAM Hα emission (blue, background) associated with the SMC, integrated between $+90$ km s^{-1} $\leqslant v_{\rm LSR} \leqslant +120$ km s^{-1}, and the MCELS Hα image (grayscale, foreground) from Winkler et al. (2015). The red box denotes the extent of the MCELS survey region. Note that the WHAM emission scaling is linear (left color bar) while scaling for the MCELS image is logarithmic (right color bar) to highlight the bright structures within the galaxy.

structures is due to difficulty in detecting the DIG in dwarf irregulars. Hunter et al. (1993) took deep Hα images of 51 irregular and amorphous galaxies, detecting emission down to a few Rayleighs[9] for the more nearby galaxies. A more recent study by Oey et al. (2007), which defined the DIG as Hα-emitting regions separate from H II regions, looked at a wide range of star-forming galaxies and found 59% $\pm$ 19% of the Hα originates from the WIM, a higher fraction than previous studies. Prior studies have generally not been very sensitive to faint DIG. However, they have been able to characterize the diffuse filamentary structure far from classical H II regions. Conversely, in our study, we are not able to exclude H II region emission in our observations of the central region of the SMC due to our beam size, which corresponds to a spatial resolution of 1 kpc at the distance of the galaxy. In the halo, this limitation does not impact our results.

In the Cosmic Origins Spectrograph (COS)/Ultraviolet and Visual Echelle Spectrograph (UVES) Absorption Survey, Fox et al. (2014) used absorption toward 69 active galactic nuclei (AGN) to push push the detection limit of the ionized gas associated with the Magellanic Clouds much lower toward regions with H I column densities of $\log N_{\rm H\,I} \approx 19.4$–$20.1$. Their target AGNs are located near the Magellanic System and along the Stream and sparsely sample the large structures. Away from the prominent 21 cm emitting structures, their lowest neutral column density sightlines ($\log N_{\rm H\,I} < 19.5$) are found to have very high ionization fractions (up to 98%).

BHB13 reported the first extended detection of DIG near the Magellanic Clouds. Their study of the Magellanic Bridge revealed that DIG traces the H I 21 cm emission, though they also found that the Hα often extends many several degrees beyond the detectable neutral hydrogen emission. Additionally, the study suggested an upper limit of 50% ionization of the gas within the Bridge system BHB13. This is similar to the general pattern in high-velocity clouds around the MW, in which the detection of Hα emission is generally correlated with the detection of H I but the intensities are not correlated (Tufte et al. 1998; Hill et al. 2009; Barger et al. 2012, 2017). If similar conditions exist within the SMC, then a large fraction of the gas has gone undetected by previous studies.

To determine if the DIG throughout the SMC has a similar ionization fraction to that of the MW and the Magellanic Bridge, we conducted an Hα emission survey of the SMC using Wisconsin Hα Mapper (WHAM). In Section 2, we describe the WHAM observations and outline our data reduction process in Section 3. We present the non-extinction corrected Hα intensity map of the SMC in Section 4 and discuss the differences and similarities of the Hα and H I emission and velocity distributions. We investigate the total mass of the SMC by addressing the distribution of neutral and ionized gas in Section 4.3. We discuss our work in Section 5 and present our conclusions in Section 6.

2. Observations

The WHAM facility was specifically designed with high sensitivity to faint optical emission lines from diffuse sources. Because the intensity of these emission lines scale with the emission measure (EM $= \int n_e^2\, dl$), the low-density gas in the galactic halos is very faint. An instrument with high sensitivity is thus necessary to observe them. The previous SMC studies listed in Section 1 detected Hα with lower intensity limit of $\sim$3–6 R, limiting observations to the central stellar region of the SMC. WHAM can detect features reliably down to $\sim$25 mR, limited primarily by foreground atmospheric lines for individual observations. However, for extended, continuous sources, WHAM has detected structures below 10 mR (Barger et al. 2012).

The spectrometer, described in detail by Haffner et al. (2003), consists of a dual-etalon Fabry–Perot spectrometer that produces a 200 km s^{-1} wide spectrum with a 12 km s^{-1} velocity resolution from light integrated over a 1° beam. Typical Hα line widths from DIG have a FWHM of $\geqslant$20 km s^{-1}, which is well-matched to WHAM's spectral resolution. A 30 s exposure can achieve a signal to noise of 20 for a 0.5 R line with a width of 20 km s^{-1}.

Observations of the SMC were taken between 2010 October 1, and 2011 January 5 at Cerro Tololo Inter-American Observatory. We Nyquist sampled the Hα emission of the SMC with WHAM at an angular resolution of 1° over the local standard of rest (LSR) velocity range of $+50 \leqslant v_{\rm LSR} \leqslant +250$ km s^{-1} from $(\ell, b) = (289\overset{\circ}{.}5, -35\overset{\circ}{.}0)$ to $(315\overset{\circ}{.}1, -55\overset{\circ}{.}3)$. Figure 2 illustrates the angular extent and spacing of a "block" of observations in the top left.

We used the observing strategy for Nyquist sampled beam spacing described by BHB13, grouping observations into "blocks" of 30–50 pointings at $0\overset{\circ}{.}5$ spacings. Each single observation had an exposure time of 30 s. Keeping exposure times short reduces the variations observed in atmospheric lines within a single block observation.

3. Data Reduction

To reduce the data, we used the ring-summing and flat-fielding procedures described in Haffner et al. (2003). After the data were ring summed, we calibrated the Hα velocities using atmospheric lines, subtracted the atmospheric emission using an atmospheric template, and calibrated the intensities to account for night-to-night differences in transmission using λ Ori as our standard intensity calibrator. These procedures are further detailed below.

[9] 1 Rayleigh $= \frac{10^6}{4\pi}$ photons s^{-1} cm^{-2} sr^{-1}.

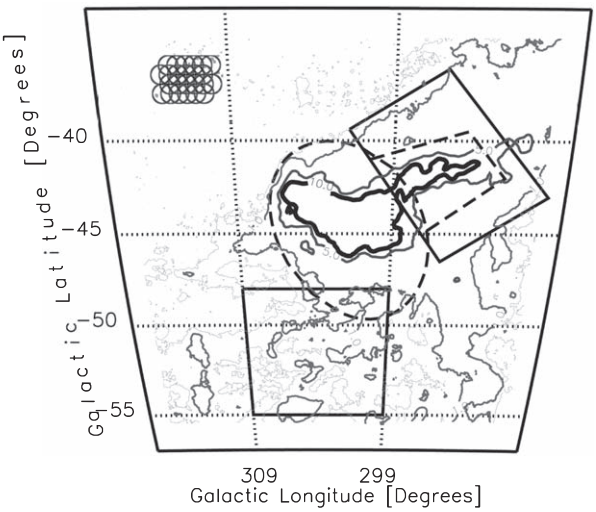

Figure 2. Full map of the SMC with each subregion highlighted. The central SMC region is marked by the dashed ellipse. The top right solid line marks the H I SMC Tail and inner dashed lines mark the Hα SMC Tail. The SMC–Stream interface region at the bottom is marked in solid black lines. The contours mark the H I column density at 0.5, 1, 5, and 10×10^{20} cm^{-2}. The grid of 1° circles at the top left of the map represent the Nyquist sampling, with points separated by 0.°5 beam steps, which were used to map the Hα emission of WHAM observations.

3.1. Data Calibration

After pre-processing the observations with the standard WHAM pipeline (Haffner et al. 2003), the spectra span a 200 km s^{-1} velocity window with 2 km s^{-1} bins in an arbitrary velocity frame. Figure 3(i) highlights the wing of the OH line, centered at a geocentric velocity of +272.44 km s^{-1}. This wing dominates the red edge of the velocity window. We use the OH line in combination with an estimated velocity shift based on multiple observations to find the velocity offset.

We assume that our background continuum level is linear over our 200 km s^{-1} window at all velocities. However, when a foreground star is present, the spectra will be elevated and contain stellar absorption lines. Beams that contain stars with $m_V < 6$ within a 0.55 radius (∼9% of our observations) are excluded from this survey to minimize this foreground contamination and are replaced with an average of the uncontaminated observations within 1°.

3.2. Bright Atmospheric Line Subtraction

Night-to-night changes in the atmosphere cause variations in the strength of the bright and faint atmospheric lines. The OH line (Meriwether 1989) is produced from interactions between solar radiation and Earth's upper atmosphere and varies in strength with the direction and the time of the observation based on the Earth–Sun geometry. Therefore, we always fit the OH line at $v_{\rm geo} = +272.44$ km s^{-1} separately from the faint atmospheric lines, which vary due to the air mass (see Section 3.3). There are two main sources that alter the shape of the bright atmospheric lines: (1) the "tuning" of the dual etalons, where the precision in aligning the dual-etalon transmission functions can have slight night-to-night variations in the instrument profile. These effects are only detectable in narrow, bright lines. (2) A geocoronal "ghost." The "ghost" lies under the lies underneath the OH line at $v_{\rm geo} = +272.44$ km s^{-1}. As described in Haffner et al. (2003), it is the result of incomplete suppression of the geocoronal line at $v_{\rm geo} = -2.3$ km s^{-1} from a neighboring order in the high-resolution etalon. In the velocity window observed in this study ($+50 \leqslant v_{\rm LSR} \leqslant +250$ km s^{-1}), some of the SMC emission may lie under the OH wing. However, because the velocity in this window only contains a portion of the OH line, it is difficult to fit well. To minimize over-subtracting the SMC emission, we assign a width of 10 km s^{-1} to the narrow OH line Gaussian fit to prevent inclusion of lower velocity emission not attributed to the OH line. However, removal of some higher-velocity SMC emission is unavoidable. We therefore integrate our emission maps over a $+90 \leqslant v_{\rm LSR} \leqslant +210$ km s^{-1} to avoid the contaminated regions. All H I emission maps and mass calculations are integrated over the same range for consistency.

3.3. Faint Atmospheric Line Subtraction

While the OH line dominates over the other atmospheric emission, faint atmospheric lines are present throughout the entire spectrum with intensities of ∼0.1 R. The strength of these lines is correlated with the air mass. BHB13 created a synthetic atmospheric spectra to describe the faint atmospheric lines observed at Cerro-Tololo International Observatory (CTIO) by observing two faint directions multiple times over a 10 day period. Properties of the atmospheric lines can be found in Table 1 and Figure 3 of BHB13, and the template creation and subtraction process is also described by Hausen et al. (2002) and Haffner et al. (2003). Our averaged spectrum consists of numerous 30 and 60 s observations, totaling 4.5 hr, toward $(\ell, b) = (60.°0, -67.°0)$ and $(89.°0, -71.°0)$. These are "faint" directions that appear to have no strong Hα emission, so the atmospheric lines can be identified. To account for changes in the flux due to the air mass and daily fluctuations, we scale the synthetic template to match the emission present in a high signal-to-noise ratio (S/N) block-averaged spectrum. We then subtract the scaled atmospheric template from the observation. The total integrated intensity of the template over the SMC window is ∼0.07 R.

3.4. Extinction Correction

3.4.1. Foreground Extinction

The Hα intensity emitted from the SMC is attenuated by foreground dust from the MW, as well as dust from within the SMC itself. To correct for foreground MW extinction, we used the method outlined in BHB13 (their Section 3.4.1):

$$I_{\rm H\alpha,corr} = I_{\rm H\alpha,obs} e^{A({\rm H\alpha})/2.5}, \quad (1)$$

where,

$$A({\rm H\alpha}) = 5.14 \times 10^{-22} \langle N_{\rm H\,I} \rangle \, {\rm cm^2 \ atoms^{-1} \ mag}. \quad (2)$$

We integrate the total H I intensity over the −100 to +100 km s^{-1} velocity range. The extinction correction is important to the mass calculations in Section 4.4. We use three different methods to estimate the mass. In one, called the ellipsoidal scenario, we calculate the extinction per beam. In the other two, we use the extinction averaged over the area to stay consistent with the mass calculation methods. Accounting for the dust attention due to the foreground materials results in a 12.9%–14.4% increase in $I_{\rm H\alpha}$ resulting from the foreground

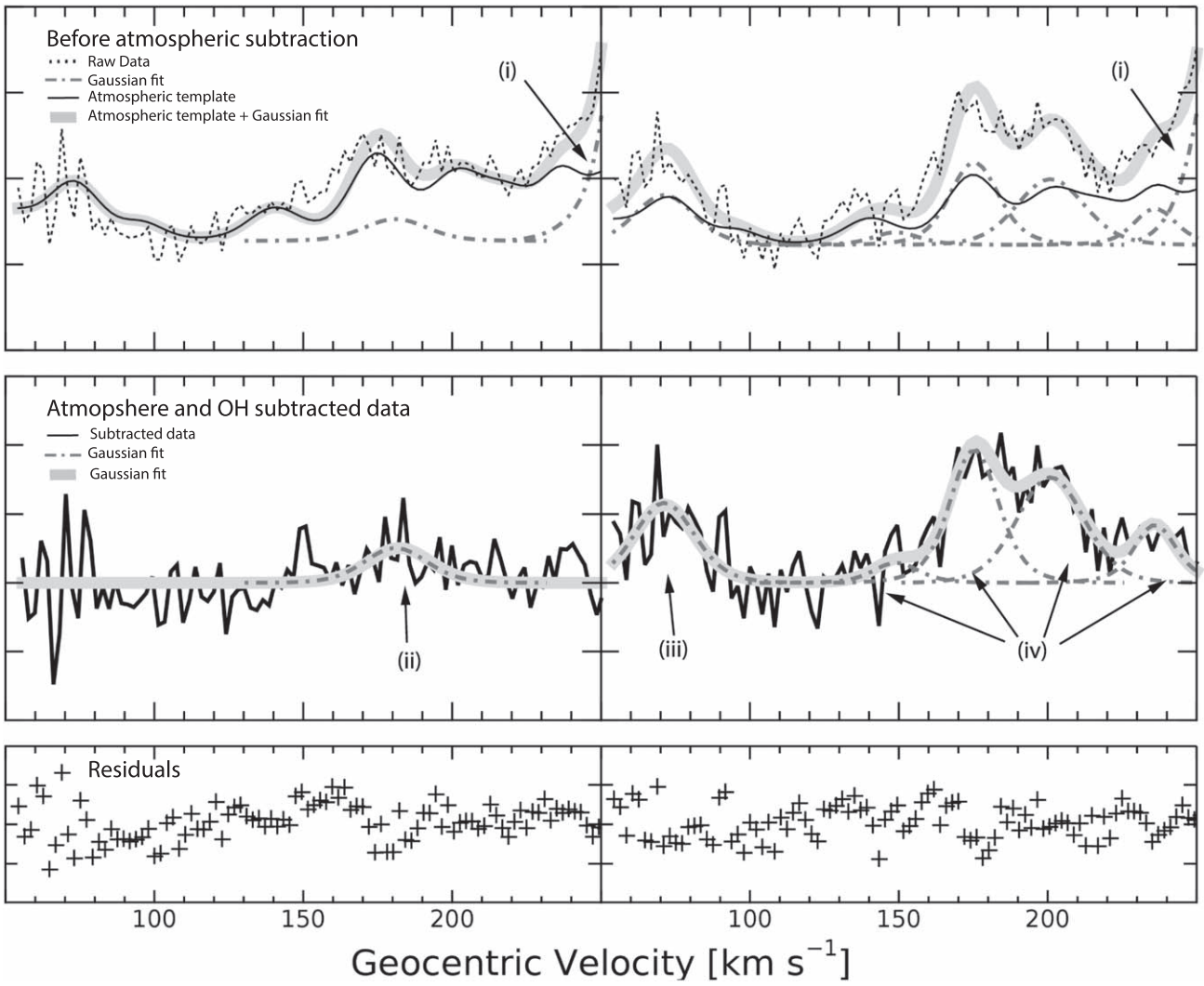

Figure 3. Example of atmospheric subtraction from a region with faint emission and a region with bright emission. The emission in the first column was taken off the SMC at $(\ell, b) = (298.^{\circ}88, -37.^{\circ}44)$. The second column was taken in a bright Hα emitting direction at $(\ell, b) = (293.^{\circ}30, -41.^{\circ}11)$. The pre-atmospheric subtracted images are shown in panels the first row. The solid black line indicates the atmospheric template (see Section 3.3), and the solid gray line marks the average fit combining the atmospheric template, the OH line fit, and emission fits. We describe our procedure for fitting the sky lines in Sections 3.2 and 3.3, with references to Hausen et al. (2002), Haffner et al. (2003), and BHB13, where the procedure is described in detail. The second row displays the post atmospheric and OH subtracted emission, with the dashed Gaussians marking fitted emission. The residuals of the subtraction are displayed in the third row. The (i) marker indicates the a bright OH line at a geocentric velocity of +272.44 km s^{-1} and (ii) indicates faint emission. Galactic emission is labeled by markers (iii). Marker (iv) indicates the bright emission from the SMC.

extinction for the SMC region, a 14.6%–16.6% and 13.7%–15.8% increase in the H I and Hα Tail regions, and a 6.4%–7.6% increase from the SMC-filament foreground (Table 1).

3.4.2. SMC Extinction

The extended envelope of the SMC has not been thoroughly studied for dust content. However, the bar of the SMC was sampled in Gordon et al. (2003). They find an $R_V = 2.74$, $A_V \backsimeq 7.6 \times 10^{-23} \langle N_{\rm H\,I} \rangle$ cm^2 mag and an average $E\ (B-V) = 0.179$ mag. To estimate the Hα extinction in the SMC, we combine Equations (1) and (4) from Gordon et al. (2003) to describe how the dust-attenuated Hα emission scales with $N_{\rm H\,I}$:

$$A(\mathrm{H}\alpha) = \left(\frac{E(\mathrm{H}\alpha - V)}{E(B-V)}\right) R_V^{-1} \langle N_{\rm H\,I} \rangle \,\mathrm{cm}^2 \ \mathrm{mag}. \quad (3)$$

We calculate the value using results listed in Gordon et al. (2003) Tables 2 and 3 for the SMC, $E(\mathrm{H}\alpha - V) = 0.197$ mag, and the resulting equation is $A(\mathrm{H}\alpha) = 1.057 \times 10^{-22} \langle N_{\rm H\,I} \rangle$ cm^2 mag. We apply the extinction correction only on the central region of the SMC for observations (or beams) with an $N_{\rm H\,I} > 1.0 \times 10^{20}$ cm^{-2} over an integrated velocity range of $+90 \leqslant v_{\rm LSR} \leqslant +210$ km s^{-1}, where the gas is coincident with the visible stellar component of the galaxy. $N_{\rm H\,I}$ is determined using the H I 4π (HI4PI) survey smoothed to 0.°25 pixels to match our angular resolution when calculating the extinction in our ellipsoidal scenario (HI4PI Collaboration et al. 2016). Our ionized skin and cylindrical scenarios use the average $N_{\rm H\,I}$ of the region to calculate the extinction for the regions in the SMC where $N_{\rm H\,I} > 1.0 \times 10^{20}$ cm^{-2}. All areas of the SMC with lower column than our cutoff were only foreground-extinction corrected. Correcting the Hα intensities for the dust within the structure results in an average

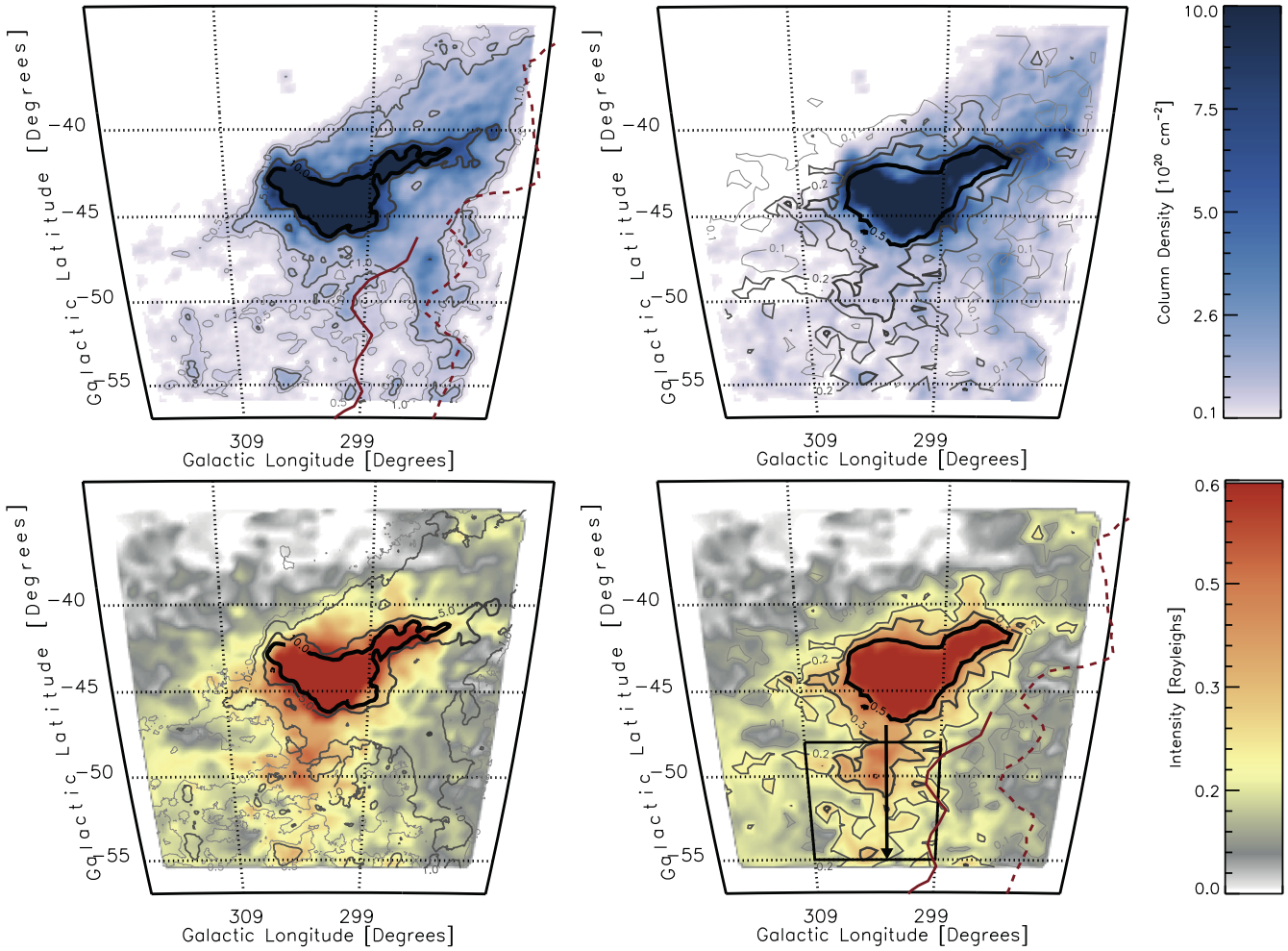

Figure 4. Comparison of H I (top row) and Hα (bottom row) emission maps from the HI4PI survey and the WHAM survey, respectively. The Hα intensity values are not extinction corrected. The left column figures present the integrated emission maps with H I contours overlaid, and the right column figures have the Hα contours overlaid. The emission for both maps is integrated over $v_{\rm LSR} = +90 \leqslant v_{\rm LSR} \leqslant +210$ km s^{-1}. The H I scaling is clipped at a column density of 10^{21} cm^{-2} to highlight the faint H I emission. The Hα emission is clipped at 0.6 R. The solid red (SMC) and dashed red (LMC) filaments mark the locations of the two H I filaments within the Magellanic Stream identified by Nidever et al. (2008). The black box marks the region that contains the SMC Hα filament, and the back arrow marks the filament from (ℓ, b) = (303.°, −47.°0) to (303.°0, −55.°0). Due to scaling limits, the SMC filament does not appear clearly in this projection.

Table 1
Extinction

Region	Foreground Extinction			Internal Extinction		
	log $\langle N_{\rm H\,I}\rangle$	A(Hα)[a]	%$_{\rm corr}$	log $\langle N_{\rm H\,I}\rangle$	A(Hα)	%$_{\rm corr}$
SMC	20.5	0.15–0.14	12.9%–14.4%	21.0	0.24–0.27[b]	20–23%
H I SMC Tail	20.6	0.17–0.20	14.6%–16.6%	20.5	0.06–0.03	6.0%–5.6%
Hα SMC Tail	20.6	0.17–0.19	13.7%–15.8%	20.7	0.11–0.6	10.0%–9.7%
SMC filament[c]	20.2	0.07–0.08	6.4%–7.6%	…	…	…

Notes.
[a] The first listed value was determined by averaging $\langle N_{\rm H\,I}\rangle$ in the region used to calculate masses in all scenarios other than the ellipsoidal scenario (see Section 4.4). The second value is a result smoothing HI4PI to a 0.°25 pixel grid similar to match the smoothed WHAM maps and was only applied to the ellipsoidal scenario.
[b] Internal extinction correction for the SMC is only applied to Hα regions, which coincide spatially with $N_{\rm H\,I} \geqslant 10.0^{20.0}$ cm^{-2}.
[c] No internal extinction values were available for the SMC filament region.

21%–23% increase for the region of the SMC where $I_{\rm H\alpha} > 0.5$ R. Because the Hα emitting regions lie throughout the SMC and not necessarily behind the full dust extent, our correction provides an upper limit for the Hα intensities.

3.5. Hα Tail and H I Tail

BHB13 included an analysis of the Hα and H I Tail of the SMC (see the region designated in Figure 2). Based on their WHAM observations, the region was integrated over

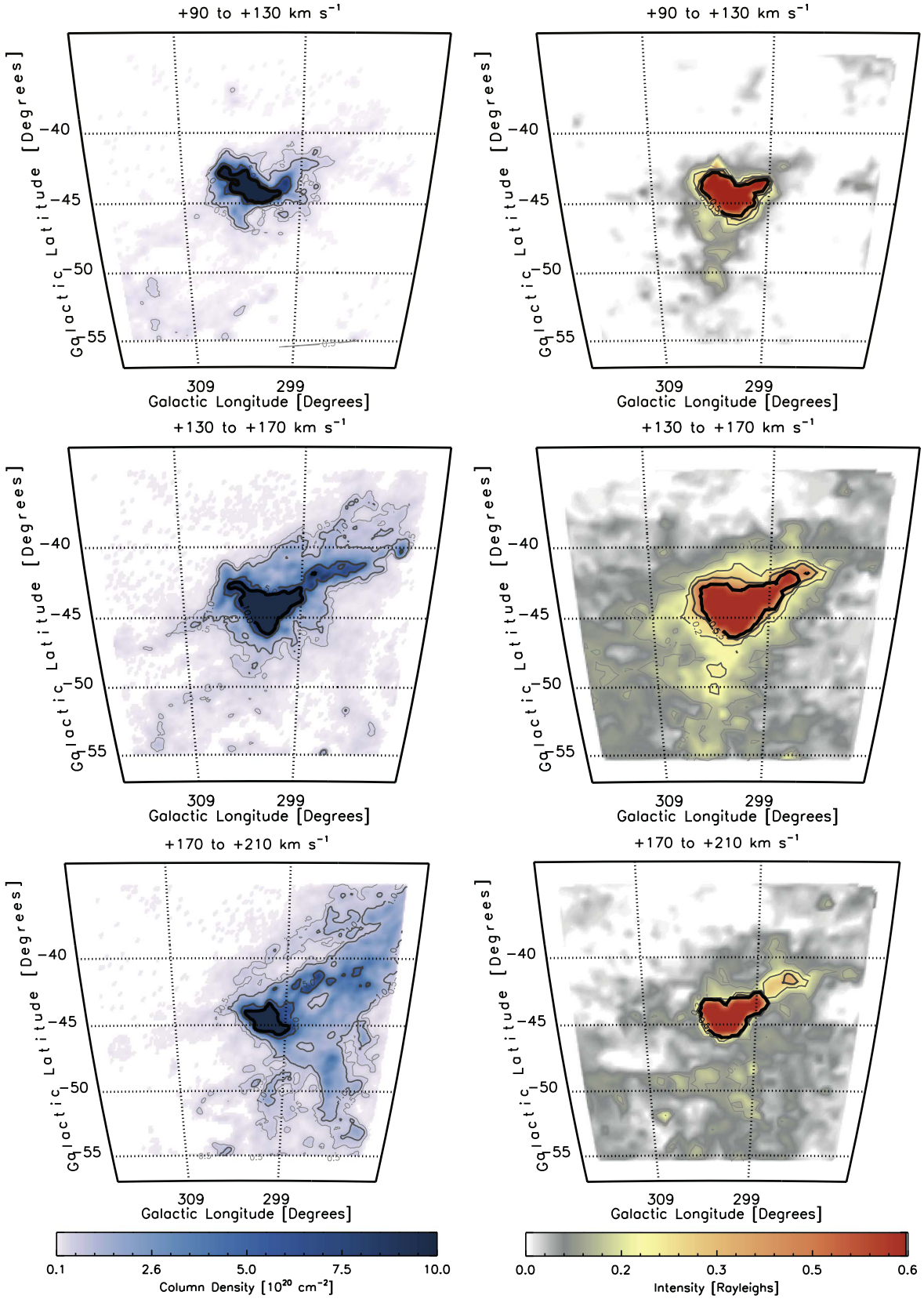

Figure 5. Comparison of H I (left column) and Hα (right column) emission maps from the HI4PI survey and the WHAM survey at different velocity channels. The H I is more compact in each channel map, while the Hα is far more extended across all velocities. Much of of the diffuse Hα extends far beyond the observable boundaries of the SMC's H I with less structural coherency than the neutral gas.

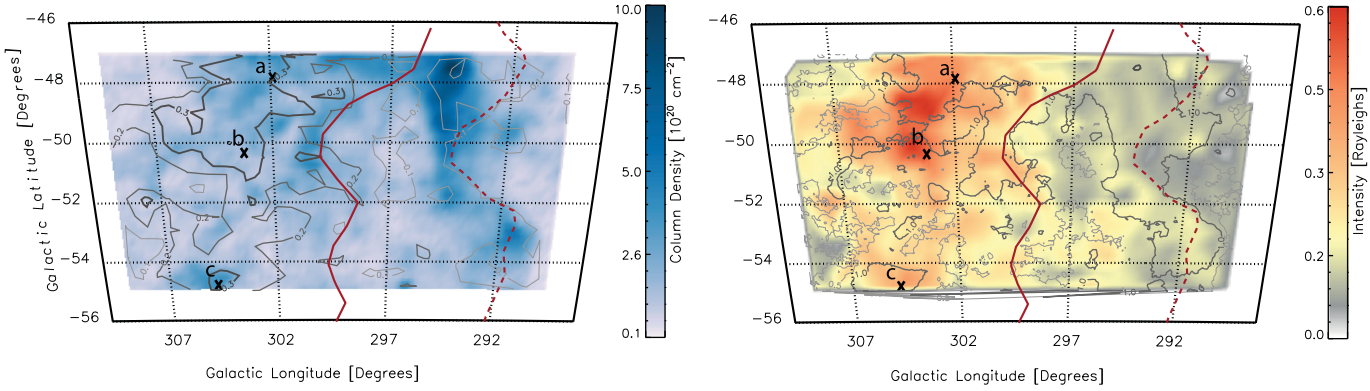

Figure 6. SMC Hα filament: H I (left) emission with Hα contours, and Hα (right) emission with H I contours overlaid. The filament runs along $l = 305°$ and extends from $b = -47°$. The solid red line traces the SMC H I filament and the dashed red line marks the LMC H I filament. Both of these filaments feed gas into the Stream and were originally kinematically traced by Nidever et al. (2008). The Hα filament appears to mirror the H I SMC filament but does not have a strong H I counterpart. The x's marked a, b, and c indicate the location of the emission fit in Figure 7.

$+100 \leqslant v_{\rm LSR} \leqslant +300$ km s^{-1}. They calculated a mass estimate using the same methods described in Section 4.4. We use an updated data reduction and intensity correction method compared to BHB13. The previous WHAM reduction pipeline included a standard 0.93 intensity correction applied universally to each night. The new pipelines calculates a night-to-night intensity variation based on the seeing conditions for a night and uses a standard calibrator (λ Ori) to calculate the transmission. In addition to the night-to-night variation, we include the transmission degradation WHAM optics in our corrections. On average, this results in a ∼20% correction to the intensity used in the BHB13.

4. Hα Intensity Map

We observed the SMC over $+50 \leqslant v_{\rm LSR} \leqslant +250$ km s^{-1}. Figure 4 displays the non-extinction-corrected total integrated intensity of the SMC in Hα and a column density map of H I. The H I and Hα map are integrated over $+90 \leqslant v_{\rm LSR} \leqslant +210$ km s^{-1} to avoid the wings of the OH line near $v_{\rm geo} = +272.44$ km s^{-1} and MW emission at $v_{\rm LSR} < +90$ km s^{-1}. The sensitivity of our survey is $I_{\rm H\alpha} \backsimeq 10$ mR, for extended continuous emission, and $I_{\rm H\alpha} \backsimeq 30$ mR for individual observations. The H I spectra were obtained from the HI4PI survey and have a sensitivity of $N_{\rm H\,I} = 2.3 \times 10^{18}$ cm^{-2} for line of 1.49 km s^{-1} wide (Ben Bekhti et al. 2016).

For the center of the galaxy, there is a strong correlation between Hα emission and $N_{\rm H\,I}$. The brightest Hα emission in the SMC traces closely the regions where $N_{\rm H\,I}$ is greater than 10^{20} cm^{-2}, with particularly strong correlation between bright Hα emission and $N_{\rm H\,I}$ of 5×10^{20} cm^{-2} and above. When compared to MCELS (Figure 1), we see the strongest emission correlates with the stellar component of the galaxy that MCELS had previously observed.

4.1. Distribution

Outside the core of the SMC, the brighter Hα emission does not appear to directly correlate with the densest H I regions. Toward the Stream, there is a bright region of Hα emission starting at $(\ell, b) = (305.^{\circ}5, -50.^{\circ}0)$ in a region we will refer to as the SMC–Stream interface. Conversely, the dense neutral filament from $b = -47°$ to $-55°$ has little Hα emission. The faint Hα emission reaches several degrees beyond the boundaries of the H I gas to the south, extending out toward the Magellanic Stream. Hα emission above 0.16 R can be

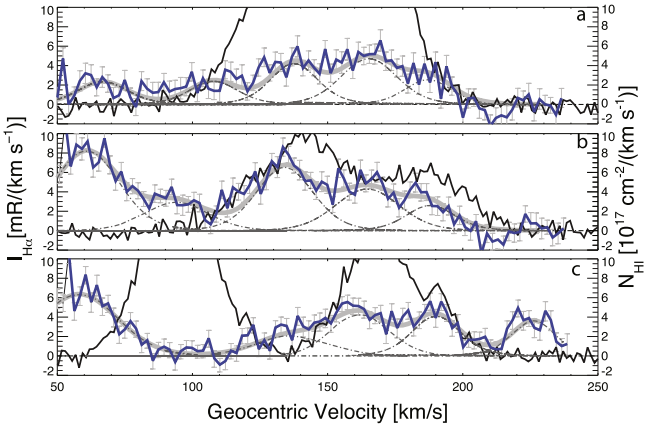

Figure 7. Three pointings from within the SMC filament. The blue lines show the Hα emission observed by WHAM, and the black lines marks the H I emission from the HI4PI survey. The dark gray contour marks the Gaussian fit to the Hα emission and the dashed Gaussians outlines the individually fit Gaussians. The location of each Gaussian is marked in Figure 6.

observed in areas without bright H I emission, such as the H I gap from $(\ell, b) = (315.^{\circ}5, -50.^{\circ}0)$ to $(307.^{\circ}0, -47.^{\circ}5)$. While WHAM is reliably sensitive to emission lines at $I_{\rm H\alpha} \geqslant 25$ mR, WHAM can detect continuous emission above 10 mR.

In Figure 5, we present $N_{\rm H\,I}$ and $I_{\rm H\alpha}$ maps at several velocity ranges, $+90 \leqslant v_{\rm LSR} \leqslant +130$ km s^{-1}, $+130 \leqslant v_{\rm LSR} \leqslant +170$ km s^{-1}, and $+170 \leqslant v_{\rm LSR} \leqslant +210$ km s^{-1}. The channel maps show the wide distribution of Hα emission at several velocities in the same spatial location. In contrast, the H I channel maps show the neutral component stays coherent in both velocity space and location.

We find a region of ionized gas extending out from the SMC, which is marked by the black box in Figure 4 (bottom right). This region begins at $(\ell, b) = (303.^{\circ}0, -47.^{\circ}0)$ and extends down to the edge of the observed region at $(303.^{\circ}0\ , -55.^{\circ}0\ )$. The ionized filament is marked by the black arrow. This ionized filament runs parallel to two neutral filaments discovered in Nidever et al. (2008), as marked by the solid red and dashed red lines. Figure 6 focuses on the region of the extended SMC containing the ionized SMC filament, with several spectra from the region in Figure 7. While there is detectable Hα on the order of 0.1 R along the H I filament marked by the solid red line, similar emission is also present in the extended region beyond the filament and does not appear

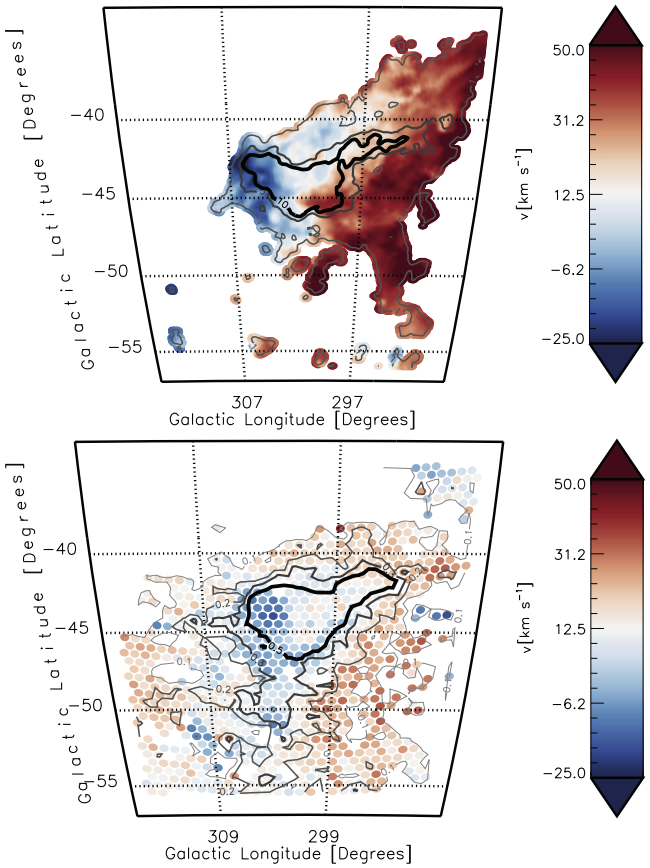

Figure 8. First moment map: the mean velocities of the gas traced by the H I (top) emission and the Hα (bottom) emission. Velocities are centered around $v_{\rm LSR} = +145$ km s^{-1}. Rotation of the ionized gas, while weaker, appears to follow the same axis as the neutral gas.

directly related to the H I filament. In contrast, along $\ell = 305°$ ionized filament, there is an Hα enhancement, with intensities of 0.2–0.5 R. This filament is spatially coincident with several H I clouds with column densities of (0.5–1.0) × 10^{20} cm^{-2}. However, no extended filamentary structure comparable to the H I filament exists at lower longitudes.

4.2. H I and Hα Velocity Distribution

Gas in the SMC has a wide velocity distribution. The first moment of the H I gas ranges from +120 km s^{-1} near the SMC–Stream interface to +190 km s^{-1} near the Bridge. These trends can be seen in Figure 8.

Previous studies have shown that the H I component has a strong gradient, suggesting that the large scale motions of the H I gas is dominated by rotation (Stanimirović et al. 2004; Di Teodoro et al. 2019). In contrast, the Hα rotation is less pronounced. We picked two pointings along the greatest velocity gradient line as measured in Stanimirović et al. (2004). Comparing mean velocities from $(\ell, b) = (299.^\circ3, -45.^\circ2)$ and $(\ell, b) = (306.^\circ0, -43.^\circ0)$, we find a velocity gradient of +67 km s^{-1} for the neutral gas and +15 km s^{-1} for the ionized gas. The appearance of weaker rotation is partially due to the broader nature of the Hα lines. WHAM measures the total integrated emission along the line of sight and cannot distinguish a singular cloud with a broad velocity range from several clouds in the halo of the galaxy imposed over clouds embedded in the interior or multiple halo clouds at different velocities. Additionally, with our 1° beam, the small scale structure is blended together. This convolution broaden the lines, shifting the mean velocity.

4.3. H^0 and H^+ Mass

We calculated the mass of ionizing gas following Hill et al. (2009) and BHB13. We assume a uniform density distribution to estimate a characteristic line-of-sight depth:

$$\mathrm{EM} = 2.75\left(\frac{T}{10^4\ \mathrm{K}}\right)^{0.924}\left(\frac{I_{\mathrm{H}\alpha}}{\mathrm{R}}\right)\mathrm{cm}^{-6}\,\mathrm{pc}. \quad (4)$$

The resulting mass in each beam is then

$$\left(\frac{M_{\mathrm{H}^+}}{M_\odot}\right) = 3.4\times10^4\,\Omega\left(\frac{D}{\mathrm{kpc}}\right)^2\left(\frac{\mathrm{EM}}{\mathrm{cm}^{-6}\,\mathrm{pc}}\right)\left(\frac{n_e}{\mathrm{cm}^{-3}}\right)^{-1}, \quad (5)$$

where n_e is the electron density, which we estimate from several scenarios described below, and Ω is the solid angle over which the mass is calculated. In our case, the solid angle is a 1° WHAM beam or a 0.°25 pixel in the resampled images. M_{H^+} is the total gas mass where H is H^+ since we include a factor of 1.4 to account for helium as in Hill et al. (2009) and BHB13. The distance to any section of the SMC is taken as the average distance of the SMC, or 60 kpc (Hilditch et al. 2005), with the exception of the SMC Tail region marked in Figure 2, where the mass is calculated with a distance of both 55 kpc and 60 kpc. All mass calculations were determined by integrating the emission over the $+90 \leqslant v_{\rm LSR} \leqslant +210$ km s^{-1} velocity range. We use the methods described in BHB13 to calculate the mass of the H I and include a factor of 1.4 to account for helium. In all cases, we smooth the H I emission to match WHAM's resolution, integrating over the same velocity range as the Hα emission.

4.4. Mass of Ionized Gas

To determine the ionized mass of the SMC and its extended system, we must make assumptions for either the line-of-sight depths or the electron density. While there are line-of-sight depths in the literature (Subramanian & Subramaniam 2009, 2012; Scowcroft et al. 2016; Ripepi et al. 2017), these depths are for the stellar component of the SMC. As is apparent from the extent of the gas, and from MW studies of the WIM, the Hα gas likely has a larger line-of-sight depth than the stellar line of sight. For our mass estimates, we assume three different scenarios. The first scenario assumes the ionized gas is in a skin around the neutral gas. For the second and third scenarios, we assume the gas is well-mixed and the H I line of sight is equal to the Hα line of sight. These line-of-sight depths must be assumed, as there is no comprehensive model of H I or Hα line-of-sight depths. Our second and third scenarios use a "cylindrical" and an "ellipsoidal" geometry, respectively. We define the third scenario as our ellipsoid scenario, where we assume a standard shape and create a model of the structure of the galaxy. For the mass calculations, we partitioned the galaxy into four different regions: the SMC Tail, the central galaxy, the SMC–Stream interface, and the extended ionized gas (Figure 2). The SMC Tail is divided into two regions in order to directly compare to deeper observations made of the same

Table 2
Neutral and Ionized Properties

Region	Neutral Properties				
	$\log \langle N_{\rm H\,I} \rangle$ ($\rm cm^{-2}$)	$M_{\rm H^0{}_{avg}}$[a] ($10^6\ M_\odot$)	$M_{\rm H^0{}_{beam}}$[b] ($10^6\ M_\odot$)	$L_{\rm H^+}$ (kpc)	$\log \langle n_0 \rangle$ ($\rm cm^{-3}$)
SMC[d]	21.0	841[c]	683[c]	9.0	−1.4
H I SMC Tail[d,g]	20.5	160–243	166–198	1.9	−1.3
Hα SMC Tail[d,g]	20.7	112–170	114–136	1.9	−1.0
SMC filament[d]	19.7	42	34	3.3	−2.3

Region	Ionized Properties					
		Ionized Skin		Cylinder	Ellipsoid	
	$\langle EM \rangle$ (10^{-3} $\rm cm^{-6}$ pc)	$L_{\rm H^+}$ (kpc)	$M_{\rm H^+}$ ($10^6 M_\odot$)	$L_{\rm H^+}$ (kpc)	$M_{\rm H^+}$ ($10^6\ M_\odot$)	$L_{\rm H^+}$ (kpc)	$M_{\rm H^+}$ ($10^6 M_\odot$)
SMC[d]	8488	6.6	738[e]	9.0	788[e]	14–20[f]	671–802[e]
H I SMC Tail[d,g]	771	0.2–0.3	26–34	1.9–2.0	74–91	1.9	76–90
Hα SMC Tail[d,g]	1284	0.1–0.1	11–14	1.9–2.0	39–48	1.9	42–50
SMC filament[d,h]	698	⋯	⋯	3.3	128	3.3	61

Notes.
[a] Mass range calculated using the column density average, applied to ionized skin and cylinder scenarios.
[b] Mass range calculated using per beam column densities, applied only to ellipsoid scenario.
[c] In all cases, our masses calculated reduces the resolution of the H I to match the WHAM resolutions. This results in an overestimation of the H I mass and our results do not match previously published results in Brüns et al. (2005).
[d] Regions defined by an ellipsoid (SMC) centered at $\ell = 301.^\circ6$ and $b = -44.^\circ8$ and polygons with the following corners: $\ell = (301.^\circ8, 295.^\circ9, 289.^\circ1, 295.^\circ7)$ and $b = (-39.^\circ4, -36.^\circ2, -43.^\circ0, -46.^\circ5)$ for the H I SMC Tail, $\ell = (300.^\circ5, 294.^\circ5, 292.^\circ0, 297.^\circ0)$ and $b = (-41.^\circ0, -39.^\circ5, -42.^\circ0, -45.^\circ0)$ for the Hα SMC Tail, and $\ell = (309.^\circ0, 299.^\circ0, 299.^\circ0, 309.^\circ0)$ and $b = (-48.^\circ0, -48.^\circ0, -55.^\circ0, -55.^\circ0)$ for the SMC filament.
[e] Not including the internal extinction of the SMC results in a mass range of $692 \times 10^6\ M_\odot$ for the ionized skin scenario, $763 \times 10^6\ M_\odot$ for the cylindrical scenario, and $(571–698) \times 10^6\ M_\odot$ for the ellipsoidal scenario.
[f] Line-of-sight depth at the maximum depth. We use 14 kpc from Subramanian & Subramaniam (2012) and 20 kpc from Scowcroft et al. (2016). Minimum depth of 3 kpc.
[g] Two different distances are used, 55 and 60 kpc. The average distance to the Bridge is 55 kpc; however, the SMC is measured at 60 kpc. Both distances are used to provide a range of possible masses and to provide a more direct comparison to results from BHB13.
[h] Ionized skin method is not applied here due to little to no H I column density.

Table 3
Ionization Mass Fraction: $M_{\rm ionized}/M_{\rm ionized+neutral}$

	Ionized Skin ($n_e = n_0$)	Cylinder	Ellipsoid
SMC	46%	48%	50%–54%
H I SMC Tail	12%–14%	27%–32%	29%–31%
Hα SMC Tail	8%–9%	22%–26%	24%–27%
SMC filament[a]	⋯	79%	65%

Note.
[a] Ionized mass fraction not calculated using $n_e = n_0$ due to little to no H I column density.

regions in BHB13. Values for each region can be found in Table 2. $M_{\rm ionized}/M_{\rm ionized+neutral}$ values are listed in Table 3.

In the first ionized skin scenario, we assume that the ionized gas lies in a skin around the H I features. This assumes a relation between the neutral gas density and the density of the electrons. This results in two possibilities, $n_e = n_0$ and $n_e = n_0/2$. If the neutral and ionized components are separated, but are in pressure equilibrium, then the electron density of an ionized skin would equal half the neutral hydrogen density (Hill et al. 2009). However, because the recombination time (∼1 Myr) is much shorter than the sound crossing time (a few hundred Myr), we expect that $n_e \approx n_0$ is more likely and only consider this case. We assume the H I column densities from HI4PI to calculate the electron column densities. This method is more reasonable outside the center of the galaxy, in regions where there is significant H I emission. Since we use the average column density over each region to calculate the mass, we use the averaged extinction over the same region to be consistent. The ionized hydrogen mass estimate for the SMC using this first method is then $\sim 7.4 \times 10^8\ M_\odot$.

Our second scenario assumes a cylindrical geometry. In this scenario, we assume $L_{\rm H^+} = L_{\rm H^0}$. This treats the ionized and neutral gas as components occupying similar mixed volumes/regions along the line of sight. In this case, the line of sight of the neutral component is similar to the line of sight of the ionized component, and each region is assumed to have the same path length, effectively a cylindrical geometry. The intensity is then averaged over the region, and treated as if it is in a single flat layer, with a depth equivalent to the width of the semimajor axis of the H I feature. This scenario uses the average extinction for the region. This results in a mass estimate of $\sim 7.9 \times 10^8\ M_\odot$.

The third scenario is our ellipsoid scenario. Similar to our cylindrical scenario, we assume that neutral and ionized gas lies along the same line of sight. However, we model the shape of the SMC as a simple ellipsoid, in order to estimate the line-of-sight depth of the gas. Similar to the BHB13 method for the Bridge, we assume that the maximum depth is equivalent to the width of the galaxy. We define the width as the semimajor axis. We chose two points on the edge of the $N_{\rm H\,I} = 1.0 \times 10^{20}\ \rm cm^{-2}$ contour to define the semimajor axis, centered at the radio kinematic center

as defined in Stanimirović et al. (2004). The projected ellipse can be seen in Figure 2, with a semimajor axis of 6 kpc and a semiminor axis of 4.55 kpc. We then assume that the line-of-sight depth of the ellipse is from 14 kpc (Subramanian & Subramaniam 2012) to 20 kpc (Scowcroft et al. 2016), based on measurements from red clump stars, RR Lyrae stars, and Cepheids. We constrained the minimum depth for the model to be no less than 1.9 kpc, again using the assumption that the width of the extended areas are similar to the depths. While there are estimates of the SMC's inclination, we chose to leave more extensive models for future work. Sightlines with intensities below 0.01 R were excluded in the mass calculations. In this scenario, we calculate the extinction correction and mass within individual smoothed 0.°25 pixels to stay consistent with the mass calculation methods. Using this model, we found the ionized content of the SMC to be $\sim 6.7 \times 10^8\ M_\odot$ using a depth of 14 kpc and $\sim 8.0 \times 10^8\ M_\odot$ using a depth of 20 kpc.

These simplified scenarios allow us to make estimates of the extended ionized gas mass but do not include many effects that would be important for higher-resolution data. The gas is more likely to be clumpy and discontinuous, with varying densities and components at different distances. These models also do not consider the inclination of the SMC nor how that would change the projected line of sight. Our calculations assumed an average distance of 60 kpc. However, gas toward the Stream is more distant, and gas toward the Bridge is closer to 55 kpc. In all regions, the H I resolution is reduced to match the WHAM resolution to consistently compare emission along the same line of sight. The results of this approximation, along with a different defined area for the galaxy, is a higher calculated H I mass than previously measured in Brüns et al. (2005). All three scenarios give $M_{\rm H^+} \sim 6 \times 10^8 M_\odot$. We do not quantify the uncertainties in the many assumptions involved, but the consistency of the estimates gives us confidence that they are realistic.

BHB13 uses neutral column densities from the Leiden/Argon/Bonn (LAB) H I survey (Kalberla et al. 2005) data set for the mass calculations of the region; here, we use HI4PI. The use of HI4PI results in ~4%–7% increase in H I in the Hα and H I Tail, which in turn decreases the mass Hα calculated for the assumed case in which we set the density of the electrons, n_e, equal to that of the neutral gas, n_0. By also included a 20% correction which accounts for degradation in the WHAM instrument and using HI4PI instead of LAB, we find similar mass results for the velocity range of $+100 \leqslant v_{\rm LSR} \leqslant +210\ {\rm km\ s^{-1}}$.

5. Discussion

5.1. SMC Filament

The trailing Magellanic Stream was first discovered by Mathewson et al. (1974). Putman et al. (2003) provided higher-resolution observations that strongly suggest a bifurcated, filamentary structure. Through a Gaussian decomposition of the H I emission, Nidever et al. (2008) traced these two filaments to the LMC and the Magellanic Bridge. The "LMC" filament is marked in Figure 4 with a dashed red line. However, the right filament in solid red has a less certain origin. Fox et al. (2010) found that quasar sightlines within the shorter filament have abundances of roughly 0.1 solar metallicity. Such measurements match the expected metallically of the SMC 2.5 Gyrs ago (Pagel & Tautvaisiene 1998; Harris & Zaritsky 2004), further suggesting an SMC origin for the filament.

The origin of the filament appears to be the lower left side of the SMC, toward the Stream, which is marked in Figure 4 (bottom right). This could suggest that the Hα filament is a shock, similar to shocks presented in Bland-Hawthorn et al. (2007). The Hα filament is near the SMC H I filament and could be the leading edge of the neutral SMC filament (solid red), pulled out similarly to the Stream filaments, and ionized by shocks. In Mastropietro et al. (2005), simulations were run with the LMC and MW, where even a low-density halo removed significant gas from the system. While the simulations did not include the SMC, if similar conditions strip gas out of the SMC, proper motions from Kallivayalil et al. (2013) suggest gas stripped would trail the SMC in the direction of the Stream. Overtime, this filament may have become more highly ionized, leaving only a few scattered H I clouds intact. Or, if the SMC has a puffy, ionized halo, interactions could be stripping outer gas directly. Confirming the extent of the Hα beyond the $b = 55°$ edge of our survey will help give a clearer picture, and line ratios could also help point to the origins of the Hα enhancement. A recent study by McClure-Griffiths et al. (2018) found a neutral outflow centered at $(\alpha, \delta) \approx 00^{\rm h}49^{\rm m}, -71°15'$, near the origin of the ionized filament. While the extent of the ionized filament is longer then the neutral outflow and offset spatially, exploring a possible relationship between the two features could help identify the origins of the structure. Extended observations of the filament is part of the ongoing WHAM Magellanic Stream Survey in Hα.

5.2. Extended SMC Gas

The diffuse ionized gas of the SMC extends beyond the traditionally defined extent of the neutral gas. The morphology, kinematics, and environment of this gas have been explored in several studies.

The COS/UVES survey compared five sightlines along the Magellanic system with WHAM observations (Fox et al. 2014). Along one sightline, FAIRALL9, they found an offset in velocity between the neutral emission at $v_{\rm LSR} = +190\ {\rm km\ s^{-1}}$ and the Hα emission at $v_{\rm LSR} = +156\ {\rm km\ s^{-1}}$, with the H$\alpha$ offset confirmed by the detection of C II* at $v_{\rm LSR} = +150\ {\rm km\ s^{-1}}$. While the location of FAIRALL9 is just outside the SMC map, we find a similar offset along a significant number of our observations for the SMC and the surrounding material, which can be seen in Figure 8. They suggest this could indicate that ionized gas exists as a boundary layer that is compressed by ram pressure as the neutral gas moves through an ionized medium. Diaz & Bekki (2011) modeled the Magellanic System and found the bifurcation of the Magellanic Stream was sensitive to drag from the hot halo, limiting the velocity dispersion of the Magellanic Stream structures. While this model is not able to reproduce the detailed kinematic and spatial structure of the Magellanic Stream, it does suggest that interactions with the surrounding coronal gas affect the morphology of the Stream. Similarly, in Barger et al. (2017), an analysis of a sample of Hα observations throughout the Stream suggests that halo–gas interactions likely affect morphology even if they are not the primary source of ionization.

The effect of the MW corona on the MCs is also discussed in Salem et al. (2015). They find the interaction between the MW coronal gas and the LMC results in a sharp drop-off in the radial gas profile. While they are not able to similarly constrain the SMC, they find that interactions with the corona would result in a truncated halo ≈3.5 kpc in size. Their study only considered the neutral gas in the SMC with a correction

for the ionized gas mass, but we find that the denser neutral gas ends more closely to the main body of the galaxy and does not extend out as far as the diffuse ionized gas. This picture is more consistent with Wang et al. (2019) as their models trace the morphology of the warm and hot gas independently from the neutral component. Modeling the formation of the Magellanic Stream and including effects of ram pressure stripping on the Clouds, they find a large, extended envelope of ionized gas while the neutral gas is concentrated near the galaxies.

Pairing the WHAM observations of the extended SMC with further absorption studies and dynamical models may help to constrain and explore the effects of the MW corona and ram pressure stripping on the system.

5.3. External Galaxies

We have measured diffuse emission in the halo of the SMC with sensitivity an order of magnitude better than other studies that have looked at the DIG in external galaxies. Observations from Rossa & Dettmar (2000) and Dettmar (1990) use a similar method to estimate the total DIG mass of edge on galaxies. In both studies, a filling factor is assumed and applied to the emission measure and a line-of-sight distance is assumed with a correction factor included for helium. The resulting masses are on the order of 10^6–10^8 $M_\odot$. For the galaxy with the largest observed diffuse gas mass, NGC 891, the total calculated diffuse gas mass is 4.0×10^8 $M_\odot$ (Dettmar 1990). This can be compared to its neutral halo mass of $M_{\mathrm{H}^0} \approx 1.2 \times 10^9$ $M_\odot$ (Oosterloo et al. 2007). In this case, the measured mass contribution of the low-ionization species is lower than the comparable neutral component. However, in our study, we are able to look through the galaxy and measure both diffuse gas in the halo as well as in the disk. In addition to the difference in sightlines, Rossa & Dettmar (2000) were able to detect the DIG down to a few Rayleighs, compared with WHAM's ∼25 mR sensitivity for singular pointings and ∼10 mR for continuous emission. To directly compare our observations to the detection limits of the previous studies, we can limit our mass calculations to bright emission. When only measuring the mass of regions with emission 5.0 R and over, which coincides with regions in the SMC with $N_{\mathrm{H\,I}} > 5.0 \times 10^{20}$ and is comparable to the extent of MCELS, we see the ionized mass of the SMC reduced by ∼50%.

Several other studies have looked at the fraction of Hα emission originating from the WIM compared to H II regions (Ferguson et al. 1996; Hoopes et al. 1996; Wang et al. 1999; Oey et al. 2007). These studies find the total contribution of Hα emission from the WIM ranges from 30% to 59%. If we use this guidance to estimate the fraction of observed emission arising from WIM within the core of the galaxy, the mass of ionized gas in this region is reduced by about 25%–45%. While we cannot separate these contributions easily due to our large beam size, such estimates still result in a substantial WIM mass for the SMC, even within its traditional boundaries.

5.4. Future Work

In this work, we present the first detection of the extended ionized halo of the SMC and the first measurements of its associated mass. While some spectra show evidence for emission outside the range we focus on ($+90 \leqslant v_{\mathrm{LSR}} \leqslant +210$ km s^{-1}), confusion with MW Hα emission and OH skyline emission prevents us from including these regions using this first data set. Nidever et al. (2008) use Gaussian decomposition to trace extended H I structures carefully through velocity regions where the Magellanic Stream blends with other sources. Combining our knowledge of MW emission from the WHAM Sky Survey (Haffner et al. 2003) and these methods may help to isolate SMC emission in the future.

While Gaussian decomposition may help with emission at lower velocities, we are limited at higher velocities due to our window only including the edge of the OH lines. BHB13 was able to recover some Magellanic emission (with reduced sensitivity) in spectra where the OH line was more completely sampled within their velocity window. We would need to obtain additional observations to attempt similar extractions in the areas of this study that are affected.

6. Summary

We have mapped the extended Hα emission of the SMC using WHAM covering a total of 546 square degrees over $+90 \leqslant v_{\mathrm{LSR}} \leqslant +210$ km s^{-1}. We compare these observations to the 21 cm emission from the HI4PI H I survey. Through these observations, we examine the extent, morphology, velocity gradients, and mass of the ionized gas. The main conclusions from our work are:

1. $N_{\mathrm{H\,I}}$ and $I_{\mathrm{H}\alpha}$ distributions. In the center of the SMC, there is a strong correlation between the $N_{\mathrm{H\,I}}$ and $I_{\mathrm{H}\alpha}$. The similar structure holds for column densities $N_{\mathrm{H\,I}} > 10^{20}$ cm^{-2}. Beyond the dense inner region, the Hα emission extends further with intensities of 0.03–0.18 R. At these intensities, there is less direct correlation with the $N_{\mathrm{H\,I}}$. This suggests there are highly ionized regions where little neutral gas remains. Of particular note is the Hα filament originating at $(\ell, b) = (305\overset{\circ}{.}5, -50\overset{\circ}{.}0)$ and extending below the galaxy. With only scattered corresponding H I clouds, this region appears to be highly ionized. This survey is limited to velocities between $+90 \leqslant v_{\mathrm{LSR}} \leqslant +210$ km s^{-1} due to atmospheric OH and MW emission contamination.
2. Velocity distribution. The rotation of the gas in the galaxy seen in $N_{\mathrm{H\,I}}$ and $I_{\mathrm{H}\alpha}$ velocity maps match well (Figure 8). This suggests the ionized gas is kinematically related to the neutral component. Although the global velocity trends agree, the intensity-weighted average Hα velocities are offset compared to the neutral gas, with the offset dependent on location. Multi-component distributions may contribute to the offset in velocity.
3. Ionized gas mass. If we assume a distance of 60 kpc, with our simplified models we find an ionized gas mass of the central SMC to be $(6.7\text{–}8.0) \times 10^8$ $M_\odot$. With a central neutral mass of $(6.8\text{–}8.4) \times 10^8$ $M_\odot$, the ionized gas appears to be roughly one half of the total atomic gas mass. The total ionized mass of all regions is $(0.8\text{–}1.0) \times 10^9$ $M_\odot$, which is comparable to the total neutral mass in the same region of $(0.9\text{–}1.1) \times 10^9$ $M_\odot$. Assumptions for n_e and line-of-sight distances dominate our uncertainty in the mass calculations.

We acknowledge the support of the U.S. National Science Foundation (NSF) for WHAM development, operations, and science activities. We thank Bob Benjamin for his comments on the manuscript. The survey observations and work presented

here were funded by NSF awards AST 1108911 and 1714472/1715623. We also thank the staff at CTIO for their continued support. We thank the referee for constructive comments that have improved the discussion in this paper.

ORCID iDs

B. M. Smart https://orcid.org/0000-0002-5012-3549
L. M. Haffner https://orcid.org/0000-0002-9947-6396
K. A. Barger https://orcid.org/0000-0001-5817-0932
A. Hill https://orcid.org/0000-0001-7301-5666

References

Barger, K. A., Haffner, L. M., & Bland-Hawthorn, J. 2013, ApJ, 771, 132
Barger, K. A., Haffner, L. M., Wakker, B. P., et al. 2012, ApJ, 761, 145
Barger, K. A., Madsen, G. J., Fox, A. J., et al. 2017, ApJ, 851, 110
Ben Bekhti, N., Flöer, L., Keller, R., et al. 2016, A&A, 594, 116
Berkhuijsen, E. M. 1998, The Volume Filling Factor of the WIM (Cambridge: Cambridge Univ. Press), 301
Besla, G., Kallivayalil, N., Hernquist, L., et al. 2007, ApJ, 668, 949
Bland-Hawthorn, J., Sutherland, R., Agertz, O., & Moore, B. 2007, ApJL, 670, L109
Brüns, C., Kerp, J., Staveley-Smith, L., et al. 2005, A&A, 432, 45
Dettmar, R. J. 1990, A&A, 232, L15
Di Teodoro, E. M., McClure-Griffiths, N. M., Jameson, K. E., et al. 2019, MNRAS, 483, 392
Diaz, J., & Bekki, K. 2011, PASA, 28, 117
Domgoergen, H., & Dettmar, R.-J. 1997, A&A, 322, 391
Ferguson, A. M. N., Wyse, R. F. G., Gallagher, J. S. I., & Hunter, D. A. 1996, AJ, 111, 2265
Fox, A. J., Wakker, B. P., Barger, K. A., et al. 2014, ApJ, 787, 147
Fox, A. J., Wakker, B. P., Smoker, J. V., et al. 2010, ApJ, 718, 1046
Gaensler, B. M., Madsen, G. J., Chatterjee, S., & Mao, S. A. 2008, PASA, 25, 184
Gardiner, L. T., & Noguchi, M. 1996, MNRAS, 278, 191
Gardiner, L. T., Sawa, T., & Fujimoto, M. 1994, MNRAS, 266, 567
Gordon, K. D., Clayton, G. C., Misselt, K. A., Landolt, A. U., & Wolff, M. J. 2003, ApJ, 594, 279
Haffner, L. M., Dettmar, R. J., Beckman, J. E., et al. 2009, RvMP, 81, 969
Haffner, L. M., Reynolds, R. J., Tufte, S. L., et al. 2003, ApJS, 149, 405
Harris, J., & Zaritsky, D. 2004, AJ, 127, 1531
Hausen, N. R., Reynolds, R. J., Haffner, L. M., et al. 2002, ApJ, 565, 1060
Hilditch, R. W., Howarth, I. D., & Harries, T. J. 2005, MNRAS, 357, 304
Hill, A., Reynolds, R., Haffner, L., Wood, K., & Madsen, G. 2012, HiA, 10, 574
Hill, A. S., Benjamin, R. A., Haffner, L. M., Gostisha, M. C., & Barger, K. A. 2014, ApJ, 787, 106
Hill, A. S., Haffner, L. M., Reynolds, R. J., et al. 2009, ApJ, 703, 1832
Hindman, J. V., McGee, R. X., Carter, A. W. L., Holmes, E. C. J., & Beard, M. 1963, AuJPh, 16, 552
HI4PI Collaboration, Ben Bekhti, N., Flöer, L., et al. 2016, A&A, 594, A116
Hoopes, C. G., Walterbos, R. A. M., & Greenwalt, B. E. 1996, AJ, 112, 1429
Hunter, D. A., & Gallagher, J. S., III 1990, ApJ, 362, 480
Hunter, D. A., & Gallagher, J. S., III 1992, ApJL, 391, L9
Hunter, D. A., Hawley, W. N., & Gallagher, J. S., III 1993, AJ, 106, 1797
Kalberla, P. M. W., Burton, W. B., Hartmann, D., et al. 2005, A&A, 440, 775
Kallivayalil, N., van der Marel, R. P., Besla, G., Anderson, J., & Alcock, C. 2013, ApJ, 764, 161
Krishnarao, D., Haffner, L. M., Benjamin, R. A., Hill, A. S., & Barger, K. A. 2017, ApJ, 838, 43
Le Coarer, E., Rosado, M., Georgelin, Y., Viale, A., & Goldes, G. 1993, A&A, 280, 365
Martin, C. L., & Kennicutt, R. C. J. 1997, ApJ, 483, 698
Mastropietro, C., Moore, B., Mayer, L., Wadsley, J., & Stadel, J. 2005, MNRAS, 363, 509
Mathewson, D. S., Cleary, M. N., & Murray, J. D. 1974, ApJ, 190, 291
McClure-Griffiths, N. M., Dénes, H., Dickey, J. M., et al. 2018, NatAs, 2, 901
Meriwether, J. W. J. 1989, JGR, 94, 14,629
Nidever, D. L., Majewski, S. R., Burton, W. B., & Nigra, L. 2010, ApJ, 723, 1618
Nidever, D. L., Majewski, S. R., & Butler Burton, W. 2008, ApJ, 679, 432
Oey, M. S., Meurer, G. R., Yelda, S., et al. 2007, ApJ, 661, 801
Oosterloo, T., Fraternali, F., & Sancisi, R. 2007, AJ, 134, 1019
Pagel, B. E. J., & Tautvaisiene, G. 1998, MNRAS, 299, 535
Putman, M. E., Staveley-Smith, L., Freeman, K. C., Gibson, B. K., & Barnes, D. G. 2003, ApJ, 586, 170
Reynolds, R. J. 1977, ApJ, 216, 433
Ripepi, V., Cioni, M.-R. L., Moretti, M. I., et al. 2017, MNRAS, 472, 808
Rossa, J., & Dettmar, R. J. 2000, A&A, 359, 433
Rossa, J., & Dettmar, R. J. 2003a, A&A, 406, 493
Rossa, J., & Dettmar, R. J. 2003b, A&A, 406, 505
Salem, M., Besla, G., Bryan, G., et al. 2015, ApJ, 815, 77
Savage, B. D., & Wakker, B. P. 2009, ApJ, 702, 1472
Scowcroft, V., Freedman, W. L., Madore, B. F., et al. 2016, ApJ, 816, 49
Stanimirovic, S., Staveley-Smith, L., Dickey, J. M., Sault, R. J., & Snowden, S. L. 1999, MNRAS, 302, 417
Stanimirović, S., Staveley-Smith, L., & Jones, P. A. 2004, ApJ, 604, 176
Subramanian, S., & Subramaniam, A. 2009, A&A, 496, 399
Subramanian, S., & Subramaniam, A. 2012, ApJ, 744, 128
Tufte, S. L., Reynolds, R. J., & Haffner, L. M. 1998, ApJ, 504, 773
Wang, J., Hammer, F., Yang, Y., et al. 2019, MNRAS, 486, 5907
Wang, J., Heckman, T. M., & Lehnert, M. D. 1999, ApJ, 515, 97
Winkler, P. F., Smith, R. C., Points, S. D., & Team, M. 2015, in ASP Conf. Ser. 491, Fifty Years of Wide Field Studies in the Southern Hemisphere: Resolved Stellar Populations of the Galactic Bulge and Magellanic Clouds, ed. S. Points & A. Kunder (San Francisco, CA: ASP), 343
Zurita, A., Rozas, M., & Beckman, J. E. 2000, A&A, 363, 9